Editors' Suggestion

Finite Temperature Phase Behavior of Viral Capsids as Oriented Particle Shells

Amit R. Singh,[1,2] Andrej Košmrlj,[3,4] and Robijn Bruinsma[5]
[1]Department of Physics and Astronomy, Johns Hopkins University, Baltimore, Maryland 21218, USA
[2]Currently at Department of Mechanical Engineering, Birla Institute of Technology and Science, Pilani, Rajasthan 333031, India
[3]Department of Mechanical and Aerospace Engineering, Princeton University, Princeton, New Jersey 08540, USA
[4]Princeton Institute for the Science and Technology of Materials (PRISM), Princeton University, Princeton, New Jersey 08544, USA
[5]Departments of Physics and Astronomy, and Chemistry and Biochemistry, University of California, Los Angeles, California 90095, USA

(Received 19 November 2019; accepted 16 March 2020; published 13 April 2020; corrected 17 April 2020)

A general phase plot is proposed for discrete particle shells that allows for thermal fluctuations of the shell geometry and of the inter-particle connectivities. The phase plot contains a first-order melting transition, a buckling transition, and a collapse transition and is used to interpret the thermodynamics of microbiological shells.

DOI: 10.1103/PhysRevLett.124.158101

The development of shells that protect microbiological systems from a hostile environment yet still allow for exchange of key nutrients was an essential step in the evolution of life [1]. These shells are composed of molecules decorated with both hydrophobic and hydrophilic groups ("amphiphiles") in such a way that in an aqueous environment they assemble into closed, semipermeable shells. An important example are the amphiphilic protein shells that surround viruses [2] as well as many bacteria and most archaea [3]. Cryogenic-based microscopy studies [2] had indicated that these "capsids" in general are strictly organized, crystallographic structures (usually icosahedral or helical) [4], but this view is being challenged. Thermodynamic studies of viral self-assembly indicate, for the case of the assembly of viruses in solutions with higher protein concentrations, that the interaction energies between capsid proteins ("subunits") should be no more than a few times the thermal energy at room temperature in order to avoid the production of malformed capsids [5–8]. Finite temperature studies also showed that, due to thermal fluctuations, at least some viral capsids are dynamical in nature and that the dynamics plays a role in the life-cycle of the virus [10,11]. Some capsids are even in a molten or "pleomorphic" state [12,13]. Finally, all-atom molecular dynamics (MD) simulations of capsids revealed that they can *collapse* under the action of thermal fluctuations [19].

The study of the melting and thermal collapse of a shell with a limited number of constituent components (10^2–10^3) is an interesting statistical physics problem in its own right. The geometry of the shell over which the components are moving itself is defined by the position vectors of these same particles and hence subject to thermal fluctuations [20]. Here, we propose a generic phase diagram for the melting and collapse of discrete shells obtained by comparing MD simulations of a coarse-grained model of capsids with the continuum theory of thermally fluctuating surfaces.

We first discuss the MD simulations. The coarse-grained model is based on the so-called oriented particle system (or "OPS") [21]. An OPS is defined as a cluster of N orientable and interacting point particles located at $\mathbf{r}_i$. An orientation-dependent pair interaction $V(\mathbf{r}_i, \mathbf{n}_i; \mathbf{r}_j, \mathbf{n}_j)$ acts between particle pairs i and j with a separation vector $\mathbf{r}_{ij} = \mathbf{r}_i - \mathbf{r}_j$ and unit vectors $\mathbf{n}_i$ and $\mathbf{n}_j$ describing their orientations [see Fig. 1 (left)]. The oriented pair interaction used in the simulations was

$$V(\mathbf{r}_i, \mathbf{n}_i; \mathbf{r}_j, \mathbf{n}_j) = V_m(1 - e^{-\alpha(|\mathbf{r}_{ij}|-a)})^2 + K|\mathbf{n}_i - \mathbf{n}_j|^2 + K[(\mathbf{n}_i + \mathbf{n}_j)\hat{\mathbf{r}}_{ij}]^2. \quad (1)$$

The first term is the Morse pair interaction [22], with binding energy V_m, equilibrium bond distance a, and potential well width $1/\alpha$. The second and third terms are

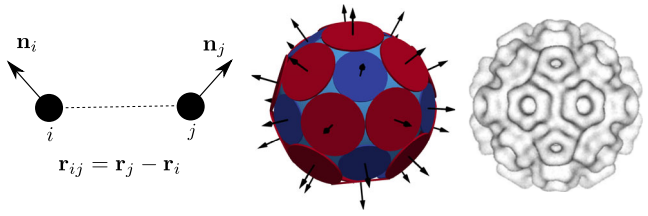

FIG. 1. Left: oriented particles i and j are separated by $\mathbf{r}_{ij} = \mathbf{r}_i - \mathbf{r}_j$ with orientations indicated by the unit vectors $\mathbf{n}_i$ and $\mathbf{n}_j$. Middle: the icosahedral groundstate configuration of an $N = 32$ oriented particle system. The particle positions are displayed as the centers of close-packed disks. The orientations are displayed as the normals to the disks. Right: micrograph of the Cowpea Chlorotic Mottle virus [23] with 32 capsomers.

known as the "conormality" and "cocircularity" terms of an OPS system. Together, these two terms are minimized if the two particles have the same orientation and if that shared orientation is perpendicular to the unit vector $\hat{\mathbf{r}}_{ij}$ that is directed along the separation vector. Only interactions between particles that are nearest neighbors are included, where the set of nearest neighbors can change over time due to thermal fluctuations.

An OPS can be viewed as a coarse-grained representation of a viral capsid by having the particle locations correspond to the centers of the "capsomers" of viral capsids. The latter are disklike groups of either six or five subunits that frequently act as the basic building blocks of a capsid [4,24]. The orientational degrees of freedom correspond to the normals to the capsomers, the depth V_m of the Morse potential to the capsomer binding energy (a few k_BT [25,26]), and the length scale a to the diameter of a capsomer (a few nanometers [2]). Because the range of the hydrophobic attraction between capsomers is short compared to their diameter, the dimensionless parameter αa characterizing the width of the Morse potential needs to be significantly larger than one. We used $\alpha a \approx 4.621$. Next, K is a measure of the bending stiffness of the shell (estimated to be in the range of $10^2 k_BT$ [27,28]). Finally, because a large energy penalty is known to obstruct the removal of single capsomers from assembled shells [29], evaporation of particles from the OPS shell is suppressed by a soft fixed-area constraint imposed via the augmented Lagrange multiplier method (see [30], Sec. I).

Figure 1 (middle) shows the minimum energy state of an $N = 32$ OPS for the case that K/V_m is large compared to one. The shell has icosahedral symmetry with the twelve blue disks indicating the five-fold symmetry sites of the icosahedron (for actual capsids, these disks would correspond to pentameric protein capsomers while the remaining 20 red disks would correspond to hexameric capsomers). This structure should be compared to that of the "$T = 3$" icosahedral pattern [4] of the 32 capsomers of the capsid of the Cowpea Chlorotic Mottle virus [23] shown in the right of Fig. 1.

Next, we carried out Brownian Dynamics simulations of $N = 72$ OPS systems using computational methods discussed further in the Supplemental Material [30] (Sec. I). The phase behavior was determined in terms of the two thermodynamic parameters $\beta^{-1} = k_BT/V_m$, a dimensionless measure of temperature in units of the depth V_m of the pair interaction, and $\gamma = 2\alpha^2 V_m R^2/(3K)$ a dimensionless measure of the inverse of the bending stiffness K ($R \sim aN^{1/2}$ is the shell radius). In continuum theory γ is known as the Föppl-von Kármán (FvK) number [39]. For different values of these two parameters we encountered ordered, molten, buckled, and collapsing shells. Representative realizations are shown in Figs. 2 and 3.

The degree of fluidity of a shell was monitored using a dynamical method based on plots of the mean square of the particle separations $\langle u^2(t)\rangle \equiv \langle |\mathbf{u}_i(t) - \mathbf{u}_j(t)|^2\rangle$ as a function of time t, averaged over all pairs (i, j) of particles that were nearest neighbors in the initial configuration [40]. For the present case, if in the long time limit $\langle u^2(t)\rangle$ saturated (on average) to a constant value much smaller than R^2 then the shell was assigned to be in a solid state. If, on the other hand, $\langle u^2(t)\rangle$ increases linearly in time until it reaches R^2—which is consistent with particle diffusion—then the shell was assigned to be in a fluid state. Finally, when plots of $\langle u^2(t)\rangle$ showed a random sequence of alternating time intervals of saturation and linear growth for a given simulation run with drastic variations between different runs then the shell was assigned to be in a fluid-solid coexistence state. Examples of these three cases are shown in Fig. 2 for $\gamma = 10.6$. In the low-temperature solid state, with $\beta^{-1} = 0.1$, the shell shape is spherical while in the coexistence regime, with $\beta^{-1} = 0.7$, significant large-scale shape fluctuations are visible. The particle array still maintains local positional order but this has largely disappeared for $\beta^{-1} = 1.6$ (fluid state).

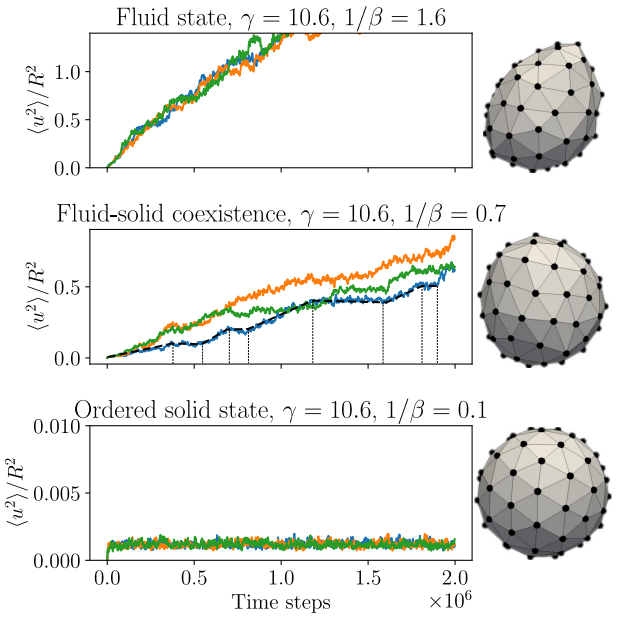

FIG. 2. Plots of the mean square $\langle u^2(t)\rangle$ of the particle displacements as a function of time for FvK number $\gamma = 10.6$ and three different temperatures β^{-1}. Three separate simulation runs are shown in each case (orange, blue, and green respectively). Bottom: for low temperatures ($\beta^{-1} = 0.1$), $\langle u^2(t)\rangle$ reaches a constant value after a short transient (ordered solid state). Top: for high temperatures ($\beta^{-1} = 1.6$), $\langle u^2(t)\rangle$ is proportional to time for the three runs, indicating diffusion (fluid state). Middle: for intermediate temperatures ($\beta^{-1} = 0.7$) the mean square displacements curves alternate between intervals where $\langle u^2(t)\rangle$ steadily increases in time and intervals where it is roughly constant (fluid-solid coexistence). The blue curve is partitioned in this manner. Snapshots on the right correspond to the final configurations for the simulation runs in blue color.

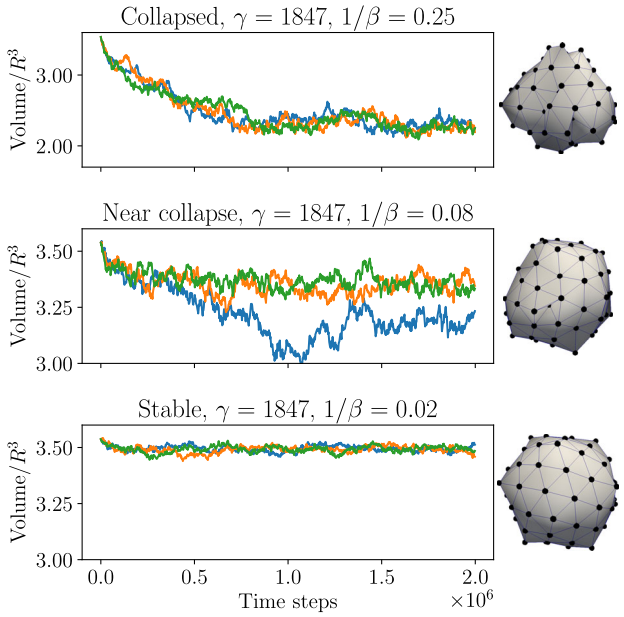

FIG. 3. Time traces of the shell volume for the FvK number $\gamma = 1847$ and three different temperatures β^{-1}. Three separate simulation runs are shown in each case (orange, blue, and green, respectively). Bottom: for low temperatures ($\beta^{-1} = 0.02$) shell volumes reach a steady state after a small initial reduction. Top: for higher temperatures ($\beta^{-1} = 0.25$) the shell volumes drastically decrease indicating the collapse of shells. Middle: for $\beta^{-1} = 0.08$ near the critical temperature for collapse, shell volumes exhibit large fluctuations and some shells undergo collapse (blue), while others remain stable (orange, green). Snapshots on the right correspond to the final configurations for the simulation runs in blue color.

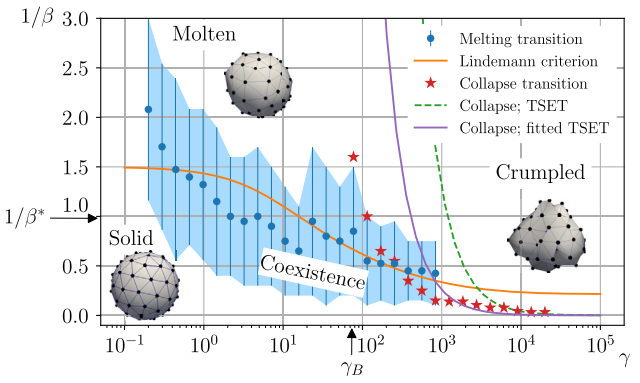

FIG. 4. Phase plot of the $N = 72$ oriented particle system. The vertical axis is the dimensionless temperature β^{-1} and the horizontal axis the FvK number γ. The KTHNY transition temperature β^{*-1} for melting of flat sheets and the buckling threshold γ_B, where the minimum energy state goes from spherical [Fig. 2(bottom)] to polyhedral [Fig. 3(bottom)], are marked by arrows. The vertical blue bars mark intervals of phase coexistence separating solid and molten states. The orange line marks the melting temperature obtained from a combination of the Lindemann criterion and thin-shell elasticity theory (TSET). The red stars mark the onset of irreversible collapse obtained from the simulations. The green dashed line marks the onset of irreversible crumpling or collapse predicted by TSET and the purple line is a fit of the TSET scaling relation with an overall numerical scale factor to account for discreteness effects.

The collapse of shells is a pronounced feature of the phase behavior of shells with larger values of the FvK number γ. Collapse was monitored by computing the volume of a continuous and differentiable surface that interpolates between the particle locations, which was constructed using the Loop shell subdivision method [41,42]. Figure 3(top) shows an example of irreversible collapse induced by thermal crumpling for $\gamma = 1847$, as indicated by a drastic reduction in volume over time and the production of very irregular shell shapes. In Fig. 3(bottom) this simulation was repeated at a reduced temperature. After a small initial reduction, the shell volume reached a steady state [43]. The low-temperature shell shape is now *icosahedral*. In Fig. 3(middle), simulations were performed near the critical temperature for collapse. In this case shell volumes exhibit large fluctuations, with some shells undergoing a first-order-like collapse transition (blue time trace), while other shells remained stable over the simulated time interval.

By collecting simulation runs for different values of the β^{-1} and γ parameters, the phase plot of Fig. 4 was produced. The vertical bars indicate temperature intervals over which fluid-solid coexistence was observed following the criterion discussed above, with the solid blue dots indicating midpoints. The large coexistence interval for small γ indicates that the melting transition should be first order on a rigid spherical surface, which is consistent with simulations of flat sheets of particles interacting via Morse potential [22]. The onset of irreversible collapse of shells for increasing temperature is indicated by orange triangles. Shells with $\gamma \gtrsim 10^3$ collapsed before the particle array could melt. On the other hand, shells with FvK numbers γ in the range of $10^2 - 10^3$ would melt with increasing temperature before they collapsed.

To interpret the phase plot, we compared it with the thin-shell elasticity theory (TSET) [44] in which a curved and stretched layer is assigned a bending and stretching energy given by

$$\mathcal{H} = \int ds \frac{\kappa}{2} H^2 + \int ds \frac{1}{2} (\lambda {u_{ii}}^2 + 2\mu {u_{ij}}^2). \qquad (2)$$

Here, κ is known as the Helfrich bending modulus of the layer, H the local mean curvature, μ and λ are two-dimensional (2D) Lamé coefficients, while u_{ij} is the strain tensor. The FvK number equals $\gamma = YR^2/\kappa$ with Y the corresponding 2D Young's modulus. For a flat sheet of point particles interacting via the Morse potential, $\lambda = \mu$ while $Y = (8/3)\mu$. In terms of the parameters of the OPS potential, $Y = 4\alpha^2 V_m/\sqrt{3}$ and $\kappa = 2\sqrt{3}K$.

According to TSET, γ determines the ground-state shape of a thin elastic shell [39] such that for γ less than a critical value γ_B (the "buckling threshold") that is in the range of 10^2–10^3, the shell has an approximately spherical shape [such as the spherical shape of Fig. 2(bottom)] while for γ above that threshold, the ground-state shape is approximately polyhedral [such as the icosahedral shape of Fig. 3(bottom)]. As indicated in the phase plot, we find a buckling threshold around $\gamma_B \simeq 75$. The discrepancy between the computed and predicted values of the buckling threshold, which has been noted before [45], is a measure of the importance of discreteness effects. To apply TSET to melting, one can combine it with the Lindemann melting criterion (LMC), which states that melting occurs when the rms of the fluctuations of particle displacements exceeds a certain fraction of the equilibrium interparticle spacing a. The LMC is known to work well for melting on flat two-dimensional surfaces [40]. In the regime of harmonic fluctuations, the mean square $\langle \vec{u}^2 \rangle$ of the in-plane fluctuations and the mean square $\langle f^2 \rangle$ of the out-of-plane fluctuations can be shown to have the scaling form $\langle \vec{u}^2 \rangle = (k_B T/Y) G^u_\infty(\gamma)$ and $\langle f^2 \rangle = (k_B T/Y) G^f_\infty(\gamma)$, respectively. The scaling functions $G^u_\infty(\gamma)$ and $G^f_\infty(\gamma)$ are discussed in the Supplemental Material [30], Sec. II. Formally, TSET theory corresponds to the limit of particle shells with N large and a small but with fixed radius $R \sim aN^{1/2}$. To include discreteness effects, we expanded the three displacement fields in terms of a series of spherical harmonics $Y_{\ell,m}$ and demanded that the total number of out-of-plane modes $\mathcal{N}(\ell_{\max}) = (\ell_{\max}+1)^2$—with $\ell_{\max}$ the maximum value of the quantum number ℓ—equals the number N of particles minus two [46]. For a shell of $N = 72$ particles $\ell_{\max} = 7$ and $\ell_{\max} = 8$ are reasonable choices (since 72 is in the interval between 8^2 and 9^2). The corrected scaling function has the same mathematical form as the TSET case but it is larger by an overall constant scale factor in the range of 10–100, depending on the value of $\ell_{\max}$: discreteness strongly amplifies the effects of thermal fluctuations. The resulting LMC melting temperatures $T_m(\gamma) = T^0_m G^u_N(0)/[G^u_N(\gamma) + G^f_N(\gamma)]$ are plotted in Fig. 4 (orange line) with the melting temperature T^0_m for $\gamma = 0$ treated as a fitting parameter [47]. The resulting fit is reasonable for the range of γ values over which melting was observed.

According to TSET, elastic shells with large γ should undergo a collapse transition with increasing temperature [48–50]. Physically, this is due to the fact that crumpled shells have a much larger configurational space for shape fluctuations than (nearly) spherical shells so their entropy is much larger as well, while the volume of a crumpled shell with fixed area is correspondingly reduced. For larger γ, the enthalpic cost of crumpling the surface is diminished so a crumpling or collapse transition is to be expected. The collapse of a shell requires overcoming a free energy barrier that according to TSET vanishes when $k_B T \gamma^{1/2}/\kappa$ is about 10^2 (green dashed line in Fig. 4 [49,50]). For the crumpling or collapse transition that we observed (red stars), solid shells (but not liquid shells) roughly obeyed this scaling relation except that the value of $k_B T \gamma^{1/2}/\kappa$ had to be decreased by a factor of about 10 (purple line in Fig. 4). We interpret this as a discreteness effect similar to the one encountered for the melting transition. In the range of $\gamma \sim 10^3 - 10^4$ the fitted thin-shell elasticity theory (purple line) provides a reasonable estimate for the collapse transition. Small discrepancies with the molecular dynamics simulation (red stars) are attributed to thermally activated escape events over the energy barrier [50]. This is reflected in the middle panel of Fig. 3, where shell volumes exhibit large fluctuations, with some shells undergoing a first-order-like collapse transition (blue time trace), while other shells remained stable over the simulated time interval. In the range of $\gamma \sim 10^2$–10^3 there is a much larger discrepancy between the thin-shell elasticity and molecular dynamics simulations. For these values of γ the collapse transition is in the same range as the melting transition. The unbound dislocation pairs that are forming during melting may significantly affect the collapse transition and this effect is not captured in the TSET.

As an example how the phase plot Fig. 4 could be applied to viral capsids, we compared the $N = 72$ OPS with what is known about the phase properties of viral capsids having 72 capsomers. It should be noted that our phase plot corresponds to empty viral capsids, while the effect of osmotic pressure due to the packaged DNA would increase both the melting and collapse temperatures due to the suppression of radial fluctuations as discussed in [49]. In the Caspar-Klug classification of capsids, icosahedral shells with 72 capsomers are known as "$T = 7$" structures [4]. Medically important $T = 7$ viruses are the human polyoma and papilloma unenveloped double-stranded DNA viruses, which both have a diameter of about 50 nm [51]. Because the polyoma and papilloma capsids are quite spherical, the value of γ should, for these two cases, lie below the buckling threshold in Fig. 4. In contrast, two forms of the capsid of the $T = 7$ thermostable DNA bacteriophage P23-45 with diameters of 66 and 82 nm are, respectively, weakly and strongly polyhedral [52]. This progression of $T = 7$ shapes straddling the buckling threshold could be understood within TSET by noting that γ scales as the square of the shell diameter. According to Fig. 4, in the relevant regime of $\beta^{-1} \simeq 1$ [5,6], capsids should be rather unstable in this part of the phase plot: prone both to melting and collapse. In actuality these viruses are known to be quite stable but this is because of a post-assembly *maturation process*, during which the capsid subunits are linked together by covalent bonds. The initial procapsids of the $T = 7$ viruses, which are not yet bonded together, still could be thermodynamically unstable. Interestingly, the assembly of the procapsids of phages typically takes place on a preformed spherical *scaffold* that

is disassembled during maturation [52]. It is very suggestive that one purpose of the scaffold is to prevent this instability. This could be checked experimentally by a study of the thermodynamic stability of self-assembling mutant $T = 7$ empty shells for which maturation and/or scaffold formation is blocked. Instability of the procapsid of the related, but much larger, $T = 13$ Herpes-Simplex virus should be even more pronounced.

We would like to thank Luigi Perotti, Jeff Eldredge and Bill Gelbart for useful discussions and the UCLA Mechanical and Aerospace Engineering Department for continued support. This work was supported by NSF through DMR Grants No. 1610384 and No. 1836404, and the CAREER Award No. DMR-1752100.

[1] B. Alberts, *Molecular Biology of the Cell* (Garland Science, New York, 2017).
[2] T. S. Baker, N. H. Olson, and S. D. Fuller, Adding the third dimension to virus life cycles: Three-dimensional reconstruction of icosahedral viruses from cryo-electron micrographs, Microbiol. Mol. Biol. Rev. **63**, 862 (1999).
[3] U. B. Sleytr, B. Schuster, E.-M. Egelseer, and D. Pum, S-layers: Principles and applications, FEM Micorbol. Rev. **38**, 823 (2014).
[4] D. L. Caspar and A. Klug, Physical principles in the construction of regular viruses, in *Cold Spring Harbor Symposia on Quantitative Biology*, Vol. 27 (Cold Spring Harbor Laboratory Press, New York, 1962), pp. 1–24.
[5] P. Ceres and A. Zlotnick, Weak protein-protein interactions are sufficient to drive assembly of Hepatitis B Virus capsids, Biochemistry **41**, 11525 (2002).
[6] S. Katen and A. Zlotnick, The thermodynamics of virus capsid assembly, Methods Enzymol. **455**, 395 (2009).
[7] H. D. Nguyen, V. S. Reddy, and C. L. Brooks III, Invariant polymorphism in virus capsid assembly, J. Am. Chem. Soc. **131**, 2606 (2009).
[8] This is due to kinetic trapping. For lower protein concentrations, the probability of kinetic trapping is reduced and interaction energies can be higher [9].
[9] E. C. Dykeman, P. G. Stockley, and R. Twarock, Solving a Levinthal's paradox for virus assembly identifies a unique antiviral strategy, Proc. Natl. Acad. Sci. U.S.A. **111**, 5361 (2014).
[10] B. Bothner, A. Schneemann, D. Marshall, V. Reddy, J. E. Johnson, and G. Siuzdak, Crystallographically identical virus capsids display different properties in solution, Nat. Struct. Mol. Biol. **6**, 114 (1999).
[11] J. A. Speir, B. Bothner, C. Qu, D. A. Willits, M. J. Young, and J. E. Johnson, Enhanced local symmetry interactions globally stabilize a mutant virus capsid that maintains infectivity and capsid dynamics, J. Virol. **80**, 3582 (2006).
[12] A. J. Battisti, Structural studies of pleomorphic viruses, Ph.D. thesis, Purdue University, 2011.
[13] The Archaeal and Bunyaviridae families of viruses (which includes the Hanta viruses) [14–16] are important examples. The Gaussian curvature of some of the Archaeal pleomorphs evolves over time [14], indicating that they are in a fluidlike state [17,18].
[14] D. Prangishvili, P. Forterre, and R. Garrett, Viruses of the Archaea: A unifying view, Nat. Rev. Microbiol. **4**, 837 (2006).
[15] A. K. Överby, R. Pettersson, K. Grünewald, and J. Huiskonen, Insights into bunyavirus architecture from electron cryotomography of Uukuniemi virus, Proc. Natl. Acad. Sci. U.S.A. **105**, 2375 (2008).
[16] M. K. Pietilä, S. Laurinavičius, J. Sund, E. Roine, and D. H. Bamford, The single-stranded DNA genome of novel archaeal virus Halorubrum pleomorphic virus 1 is enclosed in the envelope decorated with glycoprotein spikes, J. Virol. **84**, 788 (2010).
[17] L. E. Perotti, S. Dharmavaram, W. S. Klug, J. Marian, J. Rudnick, and R. F. Bruinsma, Useful scars: Physics of the capsids of archaeal viruses, Phys. Rev. E **94**, 012404 (2016).
[18] V. Vitelli, J. Lucks, and D. Nelson, Crystallography on curved surfaces, Proc. Natl. Acad. Sci. U.S.A. **103**, 12323 (2006).
[19] P. L. Freddolino, A. S. Arkhipov, S. B. Larson, A. McPherson, and K. Schulten, Molecular dynamics simulations of the complete satellite tobacco mosaic virus, Structure **14**, 437 (2006).
[20] D. Nelson and L. Peliti, Fluctuations in membranes with crystalline and hexatic order, J. Phys. (Paris) **48**, 1085 (1987).
[21] R. Szeliski and D. Tonnesen, *Surface Modeling with Oriented Particle Systems* (ACM, New York, 1992), Vol. 26.
[22] S. I. Lee and S. J. Lee, Effect of the range of the potential on two-dimensional melting, Phys. Rev. E **78**, 041504 (2008).
[23] H. Liu, C. Qu, J. E. Johnson, and D. A. Case, Pseudo-atomic models of swollen CCMV from cryo-electron microscopy data, J. Struct. Biol. **142**, 356 (2003).
[24] J. E. Johnson and J. A. Speir, Quasi-equivalent viruses: A paradigm for protein assemblies, J. Mol. Biol. **269**, 665 (1997).
[25] P. Ceres and A. Zlotnick, Weak protein-protein interactions are sufficient to drive assembly of Hepatitis B virus capsids, Biochemistry **41**, 11525 (2002).
[26] A. Zlotnick, Are weak protein–protein interactions the general rule in capsid assembly?, Virology **315**, 269 (2003).
[27] T. T. Nguyen, R. F. Bruinsma, and W. M. Gelbart, Elasticity theory and shape transitions of viral shells, Phys. Rev. E **72**, 051923 (2005).
[28] W. H. Roos, R. Bruinsma, and G. J. L. Wuite, Physical virology, Nat. Phys. **6**, 733 (2010).
[29] A. Y. Morozov, R. F. Bruinsma, and J. Rudnick, Assembly of viruses and the pseudo-law of mass action, J. Chem. Phys. **131**, 155101 (2009).
[30] See the Supplemental Material at http://link.aps.org/supplemental/10.1103/PhysRevLett.124.158101 for details of numerical methods and thin shell elasticity theory used in this work, which includes Refs. [31–38].
[31] C. Zhu, R. H. Byrd, P. Lu, and J. Nocedal, Algorithm 778: L-bfgs-b: Fortran subroutines for large-scale bound-constrained optimization, ACM Trans. Math. Softw. **23**, 550 (1997).

[32] W. Kabsch, A solution for the best rotation to relate two sets of vectors, Acta Crystallogr. A **32**, 922 (1976).
[33] V. M. Bedanov, G. V. Gadiyak, and Y. E. Lozovik, On a modified Lindemann-like criterion for 2D melting, Phys. Lett. **109**, 289 (1985).
[34] The CGAL Project, *CGAL User and Reference Manual*, 4th ed. (CGAL Editorial Board, 2019).
[35] V. Borrelli, F. Cazals, and J. M. Morvan, On the angular defect of triangulations and the pointwise approximation of curvatures, Comput. Aided Geom. Des. **20**, 319 (2003).
[36] A. R. Singh, Study of zero and finite temperature response of discrete deformable surfaces, Ph.D. thesis, UCLA, 2018.
[37] K. Shoemake, Animating rotation with quaternion curves, in *ACM SIGGRAPH Computer Graphics* (ACM, New York, 1985), Vol. 19, pp. 245–254.
[38] Z. Zhang, H. T. Davis, and D. M. Kroll, Scaling behavior of self-avoiding tethered vesicles, Phys. Rev. E **48**, R651 (1993).
[39] J. Lidmar, L. Mirny, and D. R. Nelson, Virus shapes and buckling transitions in spherical shells, Phys. Rev. E **68**, 051910 (2003).
[40] H.-H. von Grünberg, P. Keim, K. Zahn, and G. Maret, Elastic Behavior of a Two-Dimensional Crystal Near Melting, Phys. Rev. Lett. **93**, 255703 (2004).
[41] F. Cirak, M. Ortiz, and P. Schröder, Subdivision surfaces: A new paradigm for thin-shell finite-element analysis, Int. J. Numer. Methods Eng. **47**, 2039 (2000).
[42] F. Feng and W. S. Klug, Finite element modeling of lipid bilayer membranes, J. Comput. Phys. **220**, 394 (2006).
[43] Note that shape fluctuations always have to decrease the volume of shells, because the area of shells was kept fixed.
[44] H. S. Seung and D. R. Nelson, Defects in flexible membranes with crystalline order, Phys. Rev. A **38**, 1005 (1988).
[45] A. R. Singh, L. E. Perotti, R. F. Bruinsma, J. Rudnick, and W. S. Klug, Ground state instabilities of protein shells are eliminated by buckling, Soft Matter **13**, 8300 (2017).
[46] The total number of degrees of freedom is $3N - 6$, because translation and rotation are prevented.
[47] For small γ, the scaling function $G_N^f(\gamma)$ is proportional to γ while $G_N^u(\gamma)$ is constant. The reduction of the melting temperature with increasing γ is thus dominated by the out-of-plane fluctuations.
[48] J. Paulose, G. A. Vliegenthart, G. Gompper, and D. R. Nelson, Fluctuating shells under pressure, Proc. Natl. Acad. Sci. U.S.A. **109**, 19551 (2012).
[49] A. Košmrlj and D. R. Nelson, Statistical Mechanics of Thin Spherical Shells, Phys. Rev. X **7**, 011002 (2017).
[50] L. Baumgarten and J. Kierfeld, Buckling of thermally fluctuating spherical shells: Parameter renormalization and thermally activated barrier crossing, Phys. Rev. E **97**, 052801 (2018).
[51] D. M. Belnap, N. H. Olson, N. M. Cladel, W. W. Newcomb, J. C. Brown, J. W. Kreider, N. D. Christensen, and T. S. Baker, Conserved features in papillomavirus and polyomavirus capsids, J. Mol. Biol. **259**, 249 (1996).
[52] O. W. Bayfield, E. Klimuk, D. C. Winkler, E. L. Hesketh, M. Chechik, N. Cheng, E. C. Dykeman, L. Minakhin, N. A. Ranson, K. Severinov *et al.*, Cryo-em structure and in vitro dna packaging of a thermophilic virus with supersized $t = 7$ capsids, Proc. Natl. Acad. Sci. U.S.A. **116**, 3556 (2019).

Correction: The previously published Figure 2 was converted improperly during the production process and its rendition has been corrected.

Finite Temperature Phase Behavior of Viral Capsids as Oriented Particle Shells: Supplementary Material

Amit Singh[1], Andrej Košmrlj[2,3], and Robijn Bruinsma[4]
[1]*Department of Physics and Astronomy, Johns Hopkins University, Baltimore, MD 21218, USA*
[2]*Department of Mechanical and Aerospace Engineering, Princeton University, Princeton, NJ 08540, USA*
[3]*Princeton Institute for the Science and Technology of Materials (PRISM), Princeton University, Princeton, NJ 08544, USA and*
[4]*Departments of Physics and Astronomy, and Chemistry and Biochemistry, University of California, Los Angeles, CA 90095, USA*

I. NUMERICAL METHODS.

A. Variational Method

The finite temperature simulations of the OPS were based on an iterative solution of the coupled discretized Langevin equations

$$\frac{\partial U^{n+1}}{\partial \mathbf{r}_i^{n+1}} + \frac{k_B T}{D}\frac{(\mathbf{r}_i^{n+1} - \mathbf{r}_i^n)}{\Delta t} - k_B T\sqrt{\frac{2}{D\Delta t}}\boldsymbol{\xi}_i^{n+1} = 0, \tag{S1}$$

for the particle locations. At every time step, all particle locations and orientations were updated in parallel. Here, n is the time index with discrete time step Δt, $U^{n+1} = \frac{1}{2}\sum_{i\neq j} V(\mathbf{r}_i^{n+1}, \mathbf{n}_i^{n+1}; \mathbf{r}_j^{n+1}, \mathbf{n}_j^{n+1})$ the total potential energy associated with OPS pair interaction Eq. (S1) at time step $n+1$. D is the translational diffusion coefficient and the $\boldsymbol{\xi}_i^n$ are a set of $3N$ Gaussian random variables with variance one. The orientational degrees at time step $n+1$ were obtained by demanding that the torques

$$\boldsymbol{\tau}_i^{n+1} \equiv \mathbf{n}_i^{n+1} \times \frac{\partial U^{n+1}}{\partial \mathbf{n}_i^{n+1}} = 0 \tag{S2}$$

on the particle orientations vanished at every time step. Physically, "integrating-out" of the orientational degrees of freedom produces an effective interaction between the remaining translational degrees of freedom of the N point particles. The effective interaction is no longer the sum of radial pair interactions between neighboring point particles but now incudes more complex 3-body and higher-order interactions and longer-range interactions mediated by the orientational degrees of freedom.

At every time step, the set of $5N$ equations for the same number of unknowns $\mathbf{r}_i^{n+1}$ and $\mathbf{n}_i^{n+1}$ was solved by numerical minimization of the expression

$$\begin{aligned} I^{n+1} &= U^{n+1} + \left(\frac{k_B T}{2D\Delta t}\right)\sum_i \left(\mathbf{r}_i^{n+1} - \mathbf{r}_i^n\right)^2 \\ &- k_B T\sqrt{\frac{2}{D\Delta t}}\sum_i \boldsymbol{\xi}_i^{n+1}\cdot\left(\mathbf{r}_i^{n+1} - \mathbf{r}_i^n\right). \end{aligned} \tag{S3}$$

where, as before, the superscripts $n+1$ and n denote time-steps. The minimization of I^{n+1} with respect to $\mathbf{n}_i^{n+1}$ was of course restricted to rotations, which leads to Eq. (S2). The successive rotations were stored in the form of rotation vectors perpendicular to the orientation vectors. The orientations were reconstructed from the rotation vectors using the method of quaternions [1].

B. Area Constraint

In order to suppress evaporation of single particles from the cell we imposed a soft fixed area constraint using the Augmented-Lagrangian (AL) technique as follows. The constrained minimization problem is finding

the minimum of I^{n+1} subject to the constraint $A\left(\mathbf{r}^{n+1}\right) - A_0 = 0$ where A_0 is the zero-temperature area and $A\left(\mathbf{r}^{(n+1)}\right) \equiv A^{n+1}$ is the area after $n+1$ time steps. Introduce a Lagrange multiplier term and an augmenting penalty term as follows

$$F[\mathbf{r}^{(n+1)}, \mathbf{n}^{(n+1)}] = I^{n+1} + \frac{k^{n+1}}{2}\left(A^{n+1} - A_0\right)^2 - \lambda^{n+1}\left(A^{n+1} - A_0\right) \tag{S4}$$

where k^{n+1} is an estimate of the spring constant of the penalty term at time step $n+1$ and λ^{n+1} is an estimate of the Lagrange multiplier at time step $n+1$. For a given time step, successive estimates are updated according to

1. Set $k^{(n+1)} = 1000.0$ and $\lambda^{(n+1)} = 10.0$.
2. Find $\mathbf{r}^{(n+1)}, \mathbf{n}^{(n+1)} = \text{argmin } F[\mathbf{r}^{(n+1)}, \mathbf{n}^{(n+1)}]$
3. While $\left(A^{(n+1)} - A_0\right) > 10^{-8}$, repeat
   (a) $\lambda^{(n+1)} \leftarrow \lambda^{(n+1)} - k^{(n+1)}\left(A^{(n+1)} - A_0\right)$
   (b) $k^{(n+1)} \leftarrow 10 \times k^{(n+1)}$
   (c) Find $\mathbf{r}^{(n+1)}, \mathbf{n}^{(n+1)} = \text{argmin } F[\mathbf{r}^{(n+1)}, \mathbf{n}^{(n+1)}]$

At the end of this procedure the area constraint is satisfied to a desired tolerance. The advantage of Augmented Lagrangian method over the standard method of Lagrange multipliers is that one does not need to introduce an extra degree of freedom. The Augmented Lagrangian parameters k and λ are solved iteratively in a loop external to the regular time step updating. The parameter $k^{(n+1)}$ does not need to go to infinity and thus numerical ill-conditioning is avoided.

C. Simulation Details

Equation (S3) can be written in non-dimensionalized form as

$$\begin{aligned} I[\mathbf{r}^{(n+1)}, \mathbf{n}^{(n+1)}] &= \sum_{i \neq j}\left(e^{-2\alpha(|\mathbf{r}_{ij}|-a)} - 2e^{-\alpha(|\mathbf{r}_{ij}|-a)}\right) \\ &+ \frac{2\alpha^2 R^2}{3\gamma}\left(\sum_{i\neq j}|\mathbf{n}_i - \mathbf{n}_j|^2 + \sum_{i\neq j}\left(\frac{(\mathbf{n}_i + \mathbf{n}_j)\cdot\mathbf{r}_{ij}}{|\mathbf{r}_{ij}|}\right)^2\right) \\ &+ \frac{\zeta}{a^2}\frac{\left(\mathbf{r}^{(n+1)} - \mathbf{r}^{(n)}\right)^2}{2} - \frac{1}{a}\sqrt{\frac{2\zeta}{\beta}}\,\hat{\boldsymbol{\xi}}_r \cdot \left(\mathbf{r}^{(n+1)} - \mathbf{r}^{(n)}\right) \end{aligned} \tag{S5}$$

V_M, α and a are parameters of the Morse potential that control the depth, the width and the equilibrium separation respectively. R is the radius of the shell. K controls the strength of the orientational potentials. μ is the mobility. The three non-dimensional parameters are given as

$$\begin{aligned} \beta &= \frac{V_M}{k_B T}, \\ \gamma &= \frac{2\alpha^2 R^2 V_M}{3K}, \\ \zeta &= \frac{a^2}{V_M}\frac{1}{\mu\Delta t}. \end{aligned} \tag{S6}$$

The interactions between the particles are restricted to the nearest neighbors that were obtained via a triangulation of the shell surface by first projecting all particles to a sphere and then constructing the

convex hull of the particle array. The set of nearest neighbors consists of particles that share an edge in the triangulation.

The width of the Morse potential can be expressed as $\delta = \ln 2/(\alpha a)$ and we previously demonstrated that it must be larger than a critical value for the formation of stable shells at low FvK numbers. [2] In practice, we found that $\delta = 0.15$ was sufficiently large and thus we chose $\alpha a = \ln 2/0.15 = 4.621$.

We chose 30 log-spaced values of FvK number (γ) between 0.2 and 20000. For each FvK number, we used 20 temperature ($1/\beta$) values. ζ is kept fixed at 2.5×10^5. For each combination of FvK number and temperature we did 3 runs where each run comprised of evolving the system for 2×10^6 time steps starting from the zero-temperature minimum energy structure for the specific FvK number. After every time-step we "subtract" off the rigid body translation and rotation with respect to the initial structure using the Kabsch algorithm [3].

D. Simulation Output

At every time step, we stored the means of the squared relative neighbor-neighbor displacement for all particles, which is calculated as follows. Suppose that particles i and j were the nearest neighbors at time $t = 0$, then the squared relative displacement is given by $\|(\mathbf{r}_i(t) - \mathbf{r}_i(0)) - (\mathbf{r}_j(t) - \mathbf{r}_j(0))\|^2$. We cannot use displacement of individual particles $\|\mathbf{r}_i(t) - \mathbf{r}_i(0)\|^2$ because for 2D melting it diverges and relative neighbor-neighbor displacement provides the appropriate modification to the Lindemann criterion [4].

We also stored, the asphericity, the volume and the root mean-squared angle deficit of the shell. The asphericity is defined as $\langle (R_i - \langle R_i \rangle)^2 \rangle / \langle R_i \rangle^2$ where R_i is the radial distance of particle i from center of the shell. For calculating volume and root-mean-squared angle deficit, we need a triangulation of the surface of the shell defined by the particles. We calculate the triangulation by projecting each particle to a unit sphere and calculating the convex hull of the spherical point cloud using CGAL [5] software package. The angle deficit is a measure of Gaussian curvature of the surface and it is calculated as discussed in [6].

We also store the particle positions and orientations after every 2000 time steps. We use this to reconstruct the shell shape during post-processing to detect crumpling of the shells.

E. Software

The minimizations were carried out using the Limited Memory BFGS [7] algorithm and the code used is available publicly on `https://github.com/amit112amit/ops-python`, in the form of a Python wrapped C++ code. The main driver used for the simulations is `phasediagramsimulation.py` located at `https://github.com/amit112amit/ops-python/blob/master/phasediagramsimulation.py`. The results of these simulations are publicly available as an interactive Jupyter notebook at `https://mybinder.org/v2/gh/amit112amit/opsresults/master?filepath=ShowPlots.ipynb`.

II. THIN-SHELL ELASTICITY THEORY

In this section we discuss how to calculate the spectrum of in-plane and out-of-plane fluctuations within the harmonic regime of the thin-shell elasticity theory. First, we discus the continuum limit, where the radius R of the spherical shell is assumed to be much larger than its thickness t. Second, we discuss how to take into account finite size effects.

A. Large shell limit

As shown previously in refs. [8, 9], the relevant length scale for the statistical mechanics of thin shells is the elastic length scale $\ell_{\text{el}} = R\gamma^{-1/4} \sim \sqrt{Rt}$, where $\gamma = YR^2/\kappa$ is the FvK number. (Y is the Young's modulus, κ is the bending rigidity). For thin shells $\gamma \gg 1$ and thus $\ell_{\text{el}} \ll R$. In this limit it is sufficient to consider a small square patch of spherical shell, which is much larger than ℓ_{el} and much smaller than R [8, 9].

Deformation of a small spherical patch is described with displacement vector fields, which are decomposed into the outward radial displacement field $f(\mathbf{x})$ and the tangential displacements $u_i(\mathbf{x})$, where $\mathbf{x} = (x_1, x_2)$

and $i \in \{1,2\}$. The total deformation energy of a small patch consists of the bending energy cost

$$U_{\rm b} = \int dA\ \frac{1}{2}\kappa\left(\Delta f\right)^2, \tag{S7}$$

where κ is the bending rigidity, and the stretching energy cost

$$U_{\rm s} = \int dA\left[\frac{1}{2}\lambda u_{ii}^2 + \mu u_{ij}^2\right], \tag{S8}$$

where λ and μ are Lame elastic constants with the Young's modulus $Y = 4\mu(\mu+\lambda)/(2\mu+\lambda)$ and the summation over repeated indices is implied. Here, we introduced the strain tensor

$$u_{ij} = \frac{1}{2}\left(\partial_i u_j + \partial_j u_i\right) + \delta_{ij}\ \frac{f}{R}, \tag{S9}$$

where δ_{ij} is the Kronecker delta. Since we are only focusing on the harmonic spectrum of fluctuations, we neglected the nonlinear term $(\partial_i f)(\partial_j f)/2$ in the strain tensor u_{ij}, which becomes relevant, when the amplitude of fluctuations becomes larger than the shell thickness [9].

The spectrum of fluctuations can be analyzed with the help of Fourier transforms $f(\mathbf{x}) = \sum_{\mathbf{q}} f(\mathbf{q})e^{i\mathbf{q}\cdot\mathbf{x}}$ and $u_i(\mathbf{x}) = \sum_{\mathbf{q}} u_i(\mathbf{q})e^{i\mathbf{q}\cdot\mathbf{x}}$. Furthermore, we use the Helmholtz decomposition for the in-plane displacements $\mathbf{u}(\mathbf{q}) = \mathbf{u}_\parallel(\mathbf{q}) + \mathbf{u}_\perp(\mathbf{q})$, where $\mathbf{u}_\parallel \parallel \mathbf{q}$ and $\mathbf{u}_\perp \perp \mathbf{q}$. Using this decomposition we rewrite the total deformation energy as

$$\begin{aligned} U_{\rm b} + U_{\rm s} = A\sum_{\mathbf{q}}\Bigg(&\frac{1}{2}\kappa q^4|f(\mathbf{q})|^2 + \frac{1}{2}(2\mu+\lambda)q^2|\mathbf{u}_\parallel(\mathbf{q})|^2 + \frac{1}{2}\mu q^2|\mathbf{u}_\perp(\mathbf{q})|^2 + 2\frac{(\mu+\lambda)}{R^2}|f(\mathbf{q})|^2 \\ &+ i\frac{(\mu+\lambda)}{R}\left[\mathbf{q}\cdot\mathbf{u}_\parallel(\mathbf{q})\right]f(-\mathbf{q}) - i\frac{(\mu+\lambda)}{R}\left[\mathbf{q}\cdot\mathbf{u}_\parallel(-\mathbf{q})\right]f(\mathbf{q})\Bigg). \end{aligned} \tag{S10}$$

The spectrum of thermal fluctuations is thus

$$\left\langle|f(\mathbf{q})|^2\right\rangle = \frac{k_B T}{A(\kappa q^4 + Y/R^2)}, \tag{S11a}$$

$$\left\langle|\mathbf{u}_\perp(\mathbf{q})|^2\right\rangle = \frac{k_B T}{A\mu q^2}, \tag{S11b}$$

$$\left\langle|\mathbf{u}_\parallel(\mathbf{q})|^2\right\rangle = \frac{k_B T(4(\mu+\lambda)+\kappa q^4 R^2)}{A(Yq^2+\kappa q^6 R^2)(2\mu+\lambda)}, \tag{S11c}$$

where T is temperature, k_B the Boltzmann constant, and A the area of the small spherical patch. The total amplitude of out-of-plane fluctuations can then be obtained as

$$\left\langle f(\mathbf{x})^2\right\rangle = \sum_{\mathbf{q}}\left\langle|f(\mathbf{q})|^2\right\rangle \approx A\int\frac{d^2\mathbf{q}}{(2\pi)^2}\left\langle|f(\mathbf{q})|^2\right\rangle \approx A\int_{\pi/R}^{\pi/a}\frac{qdq}{(2\pi)}\left\langle|f(q)|^2\right\rangle \equiv \frac{k_B T}{Y}G_\infty^f(\gamma), \tag{S12a}$$

$$G_\infty^f(\gamma) \approx \begin{cases} \sqrt{\gamma}/(2\pi), & a \ll \ell_{el} \ll R \\ (\pi/4)(R/a)^2, & \ell_{el} \ll a \ll R \end{cases}, \tag{S12b}$$

where a is the microscopic cutoff related to the interparticle spacing. Similarly, we calculate the total amplitude of in-plane fluctuations as

$$\left\langle\mathbf{u}(\mathbf{x})^2\right\rangle = \sum_{\mathbf{q}}\left(\left\langle|\mathbf{u}_\parallel(\mathbf{q})|^2\right\rangle + \left\langle|\mathbf{u}_\perp(\mathbf{q})|^2\right\rangle\right) \approx A\int_{\pi/R}^{\pi/a}\frac{qdq}{(2\pi)}\left(\left\langle|\mathbf{u}_\parallel(q)|^2\right\rangle + \left\langle|\mathbf{u}_\perp(q)|^2\right\rangle\right) \equiv \frac{k_B T}{Y}G_\infty^u(\gamma), \tag{S13a}$$

$$G_\infty^u(\gamma) \approx \begin{cases} (2/9\pi)\left[\ln(\gamma) + 8\ln(R/a)\right], & a \ll \ell_{el} \ll R \\ (8/3\pi)\ln(R/a) & \ell_{el} \ll a \ll R \end{cases}, \tag{S13b}$$

where we used $\mu = \lambda = 3Y/8$ that corresponds to the continuum limit of the OPS.

B. Finite size effects

In order to capture the finite size effects for small shells composed of N particles, we have to consider deformations of the whole spherical shell, which are decomposed into the outward radial displacement field $f(\theta,\phi)$ and the tangential displacements $u_\alpha(\theta,\phi)$, where $\alpha \in \{\theta,\phi\}$. The Helmholtz decomposition is used for tangential displacements to separate the irrotational and the solenoidal part as [10]

$$u_\alpha = D_\alpha \psi + \gamma_{\alpha\beta} D^\beta \chi. \tag{S14}$$

Here D_α are covariant derivatives and $\gamma_{\alpha\beta}$ is the alternating tensor, which depends on the metric and can be expressed as $\gamma_{\alpha\beta} = \sqrt{g}\epsilon_{\alpha\beta}$, where g is the determinant of the metric tensor $g_{\alpha\beta}$ and $\epsilon_{\alpha\beta}$ is the antisymmetric Levi-Civita symbol. Indices are raised and lowered with the metric tensor $g_{\alpha\beta}$. The tangential displacements can thus be described with two fields $\psi(\theta,\phi)$ and $\chi(\theta,\phi)$. The 3 scalar fields describing displacements can be expanded in spherical harmonics as

$$\begin{aligned} f(\theta,\phi) &= r_0 + \sum_{\ell=2}^{\ell_{\max}} \sum_{m=-\ell}^{\ell} a_{\ell,m}\ R\ \mathrm{Y}_{\ell,m}(\theta,\phi), \\ \psi(\theta,\phi) &= \sum_{\ell=2}^{\ell_{\max}} \sum_{m=-\ell}^{\ell} b_{\ell,m}\ R^2\ \mathrm{Y}_{\ell,m}(\theta,\phi), \\ \chi(\theta,\phi) &= \sum_{\ell=2}^{\ell_{\max}} \sum_{m=-\ell}^{\ell} c_{\ell,m}\ R^2\ \mathrm{Y}_{\ell,m}(\theta,\phi). \end{aligned} \tag{S15}$$

Note that we excluded spherical harmonics with $\ell = 1$ that generate translations. The radial shrinking of shell r_0 is obtained from the fixed area constraint as

$$r_0 = -\frac{R}{16\pi} \sum_{\ell=1}^{\ell_{\max}} \sum_{m=-\ell}^{\ell} (\ell^2+\ell+2)|a_{\ell,m}|^2. \tag{S16}$$

The cutoff $\ell_{\max}$ is determined by requiring that the total number of degree of freedoms $3(\ell_{\max}+1)^2$ is equal to $3N-6$, where the 6 degrees of freedom are subtracted to prevent translations and translations. For a shell with $N = 72$ particles we consider $\ell_{\max} = 7$ and $\ell_{\max} = 8$.

The total deformation energy can be rewritten as [10]

$$\begin{aligned} U_\mathrm{b} + U_\mathrm{s} = \int dA \Bigg[& \frac{\kappa}{2}\left(\Delta f + \frac{2f}{R^2}\right)^2 + 2(\mu+\lambda)\frac{f^2}{R^2} + 2(\mu+\lambda)\left(\Delta\psi\right)\frac{f}{R} \\ & + \frac{(2\mu+\lambda)}{2}\left(\Delta\psi\right)^2 + \mu\frac{\psi\left(\Delta\psi\right)}{R^2} + \frac{\mu}{2}\left(\Delta\chi\right)^2 + \mu\frac{\chi\left(\Delta\chi\right)}{R^2}\Bigg]. \end{aligned}$$

$$\begin{aligned} U_\mathrm{b} + U_\mathrm{s} = \sum_{\ell=1}^{\ell_{\max}} \sum_{m=-\ell}^{\ell} \Bigg[& \left(\frac{\kappa}{2}(\ell+2)^2(\ell-1)^2 + 2(\mu+\lambda)R^2\right)|a_{\ell,m}|^2 - (\mu+\lambda)R^2\,\ell(\ell+1)\left(a_{\ell,m}b^*_{\ell,m} + a^*_{\ell,m}b_{\ell,m}\right) \\ & + \frac{R^2\ell(\ell+1)}{2}\left[(2\mu+\lambda)\ell(\ell+1) - 2\mu\right]|b_{\ell,m}|^2 + \frac{\mu R^2}{2}(\ell-1)\ell(\ell+1)(\ell+2)|c_{\ell,m}|^2\Bigg]. \end{aligned} \tag{S17}$$

The spectrum of fluctuations is thus

$$\begin{aligned} \left\langle |a_{\ell,m}|^2 \right\rangle &= \frac{k_B T}{\kappa(\ell+2)^2(\ell-1)^2 + YR^2\frac{(\ell+2)(\ell-1)}{\ell(\ell+1)-2\mu/(2\mu+\lambda)}}, \\ \left\langle |b_{\ell,m}|^2 \right\rangle &= \frac{k_B T}{(2\mu+\lambda)R^2\ell^2(\ell+1)^2 - 2\mu R^2\ell(\ell+1) - \frac{4(\mu+\lambda)^2R^4\ell^2(\ell+1)^2}{[\kappa(\ell+2)^2(\ell-1)^2+4(\mu+\lambda)R^2]}}, \\ \left\langle |c_{\ell,m}|^2 \right\rangle &= \frac{k_B T}{\mu R^2(\ell-1)\ell(\ell+1)(\ell+2)}. \end{aligned} \tag{S18}$$

The variance of radial fluctuations is

$$\langle \delta f^2 \rangle = \sum_{\ell=2}^{\ell_{\max}} \sum_{m=-\ell}^{\ell} R^2 \langle |a_{\ell,m}|^2 \rangle \equiv \frac{k_B T}{Y} G_N^f(\gamma),$$
$$G_N^f(\gamma) = \sum_{\ell=2}^{\ell_{\max}} \sum_{m=-\ell}^{\ell} \frac{\gamma}{(\ell+2)^2(\ell-1)^2 + \gamma \frac{(\ell+2)(\ell-1)}{\ell(\ell+1)-2/3}}, \tag{S19}$$

where we used $\mu = \lambda = 3Y/8$ that corresponds to the continuum limit of the OPS. Similarly, we calculate the variance of tangential fluctuations as

$$\langle \mathbf{u}^2 \rangle = \sum_{\ell=1}^{\ell_{\max}} \sum_{m=-\ell}^{\ell} R^2 \, \ell(\ell+1) \left[\langle |b_{\ell,m}|^2 \rangle + \langle |c_{\ell,m}|^2 \rangle \right] \equiv \frac{k_B T}{Y} G_N^u(\gamma),$$
$$G_N^u(\gamma) = \sum_{\ell=2}^{\ell_{\max}} \sum_{m=-\ell}^{\ell} \left(\frac{8}{3\left[3\ell^2(\ell+1)^2 - 2\ell(\ell+1) - \frac{6\gamma\ell^2(\ell+1)^2}{(3\gamma+(\ell+2)^2(\ell-1)^2)} \right]} + \frac{8}{3(\ell-1)\ell(\ell+1)(\ell+2)} \right) \tag{S20}$$

In Fig. S1 we compare the scaling functions for radial displacements $G_N^f(\gamma)$ in Eq. (S19) and tangential displacements $G_N^u(\gamma)$ in Eq. (S20) for a shell with $N = 72$ particles ($\ell_{\max}$ = 7-8) to the ones obtained in the large shell limit ($G_\infty^f(\gamma)$ and $G_\infty^f(\gamma)$ in Eqs. (S12) and (S13) with $R/a = 2.2$). The radius $R = 2.2a$ was chosen, such that the area of the sphere is equal to the area of 140 equilateral triangles with side length a that are covering the surface of the shell with $N = 72$ particles, i.e. $4\pi R^2 = 140a^2\sqrt{3}/4$. Because the shell radius is quite small, we didn't use asymptotic expressions in Eqs. (S12b) and (S13b), but we numerically integrated expressions in Eqs. (S12a) and (S13a).

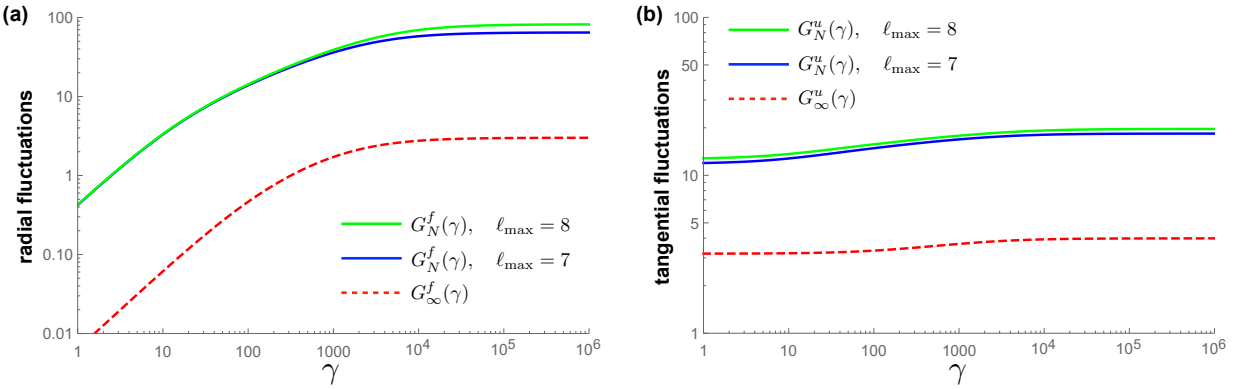

FIG. S1. Comparison of (a) radial fluctuations and (b) tangential fluctuations between the continuum theory for large thin shells (red dashed lines, $R/a = 2.2$) and finite size shells (blue, $\ell_{\max} = 7$, and green, $\ell_{\max} = 8$).

[1] K. Shoemake, "Animating rotation with quaternion curves," in *ACM SIGGRAPH computer graphics*, Vol. 19 (ACM, 1985) pp. 245–254.

[2] A. R. Singh, *Study of Zero and Finite Temperature Response of Discrete Deformable Surfaces*, Ph.D. thesis, UCLA (2018).

[3] W. Kabsch, "A solution for the best rotation to relate two sets of vectors," Acta Crystallogr. A **32**, 922–923 (1976).

[4] V. M. Bedanov, G. V. Gadiyak, and Y. E. Lozovik, "On a modified lindemann-like criterion for 2d melting," Phys. Lett. **109**, 289–291 (1985).

[5] The CGAL Project, *CGAL User and Reference Manual*, 4.14.1 ed. (CGAL Editorial Board, 2019).

[6] V. Borrelli, F. Cazals, and J. M. Morvan, "On the angular defect of triangulations and the pointwise approximation of curvatures," Comput. Aided Geom. Des. **20**, 319–341 (2003).

[7] C. Zhu, R. H. Byrd, P. Lu, and J. Nocedal, "Algorithm 778: L-bfgs-b: Fortran subroutines for large-scale bound-constrained optimization," ACM Trans. Math. Softw. **23**, 550–560 (1997).
[8] J. Paulose, G. A. Vliegenthart, G. Gompper, and D. R. Nelson, "Fluctuating shells under pressure," Proc. Natl. Acad. Sci. U.S.A. **109**, 19551–19556 (2012).
[9] A. Košmrlj and D. R. Nelson, "Statistical mechanics of thin spherical shells," Phys. Rev. X **7**, 011002 (2017).
[10] Z. Zhang, H. T. Davis, and D. M. Kroll, "Scaling behavior of self-avoiding tethered vesicles," Phys. Rev. E **48**, R651 (1993).